INVESTIGATION OF DIRECT FORCE CONTROL FOR PLANETARY AEROCAPTURE AT NEPTUNE

Rohan G. Deshmukh,[*] **Soumyo Dutta,**[†] **and David A. Spencer**[‡]

In this work, a direct force control numerical predictor-corrector guidance architecture is developed to enable Neptune aerocapture using flight-heritage blunt body aeroshells. A linear aerodynamics model is formulated for a Mars Science Laboratory-derived aeroshell. The application of calculus of variations shows that the optimal angle of attack and side-slip angle control laws are bang-bang. A closed-loop numerical predictor-corrector direct force control guidance algorithm is developed and numerically simulated using the Program to Optimize Simulated Trajectories II. The Monte Carlo simulated trajectories are demonstrated to be robust to the modeled dispersions in aerodynamics, atmospheric density, and entry state. An aerocapture technology trade study demonstrates that blunt body direct force control aerocapture enables similar performance as slender body bank angle control but halves the peak g-loading.

INTRODUCTION

Missions to the Neptune system can enable fundamental science regarding the formation of the solar system. To date, Voyager 2 is the only spacecraft to approach the distant ice giant, with a 1979 flyby of Neptune at a closest approach altitude of 4,950 km. The design of an orbital mission at Neptune is challenging, due to the velocity change required to capture. For an entry velocity of 29 km/s, the amount of dissipated orbital velocity needed to achieve a stable science orbit is about 5.5 km/s. Chemical propellant could be utilized to provide the necessary orbit insertion maneuver, but the propellant would constitute a significant amount of the mass of the flight system. To alleviate much of the propellant cost, aerocapture has been recently envisioned as the desired orbit insertion technique at Neptune.

As illustrated in Figure 1, aerocapture utilizes aerodynamics forces generated during atmospheric flight to dissipate enough hyperbolic orbital energy such that the trajectory captures into a desired orbit. For a science mission, the desired orbit can be parameterized by the radius of periapsis, r_p^t, and apoapsis, r_a^t, as well as orbit inclination, i^t, and longitude of ascending node, LAN^t. During the single atmospheric pass, the guidance system actively controls the vehicle such that both the vehicle's aeroshell heating and loading limits are regulated as the desired orbit is achieved at atmospheric exit. Errors in the trajectory targeting are corrected using propulsive burns.

---

[*] Graduate Research Assistant, School of Aeronautics and Astronautics, Purdue University, 480 W Stadium Ave.
[†] Aerospace Engineer, Atmospheric Flight and Entry Systems Branch, NASA Langley Research Center, 1 Nasa Dr.
[‡] Associate Professor, School of Aeronautics and Astronautics, Purdue University, 480 W Stadium Ave.
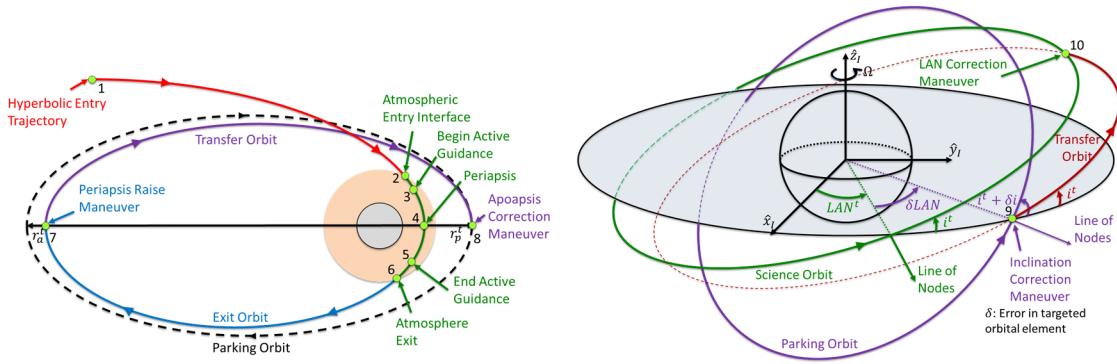
Figure 1. Aerocapture orbit insertion technique where planetary atmosphere is utilized to capture a hyperbolic entry trajectory into a desired orbit. Four propulsive burns to correct periapsis and apoapsis radius, inclination, and longitude of ascending node represent the total orbit insertion cost.

Although not flight-proven, Neptune mission architectures employing aerocapture have been studied in literature. In 2005, the National Aeronautics and Space Administration (NASA) conducted an inter-center systems analysis of Neptune aerocapture to assess feasibility, benefit and risk of an aeroshell aerocapture system, and identify technology gaps and performance goals.[1,2] The study concluded that aerocapture can enable a 1.4 times increase in delivered mass-to-orbit than an all propulsive mission for the same launch vehicle. A critical architectural assumption utilized by the study was selecting higher lift-to-drag ratio (L/D) vehicles over flight-heritage blunt body vehicles. Despite the rationale of achieving "reasonable theoretical corridor widths for aerocapture into high energy elliptical orbit", the study does not demonstrate why low L/D vehicle cannot be utilized. A potential reason for this conclusion is the reliance on the bank angle flight control technique for the vehicle's guidance. This restricts the aerodynamic maneuverability of the vehicle due to its static L/D, and hence limits resilience to atmospheric uncertainties. Furthermore, the study identified two strongly enhancing technologies needed for Neptune aerocapture: 1) aerocapture guidance algorithm and 2) angle of attack modulation.

Entry guidance algorithms drive the robustness and performance of aerocapture. The three categories of studied algorithms include reference-based, analytic predictor-corrector, and numerical predictor-corrector. Reference-based tracking algorithms, including derivatives from Apollo skip entry guidance[3], rely on steering the vehicle along predetermined reference trajectory, whose performance can be significantly influenced by day-of-flight uncertainties. Analytical predictor-correctors, such as the hybrid predictor-corrector aerocapture scheme used in the Neptune aerocapture study[4], utilize analytical solutions to the atmospheric flight equations of motion to predict the trajectory, altitude rate and orbit plane feedback for apoapsis and inclination targeting, and sensed acceleration for on-board atmospheric density model updates to account for trajectory dispersions.[5] Lastly, numerical predictor-correctors fully integrate the equations of motion and utilize numerical optimization techniques to provide higher accuracy while potentially increasing the computational expense. With the advancements in on-board computational power, the algorithm has potential applicability to outperform their analytical counterparts and thus has seen much recent investigation in literature.[6,7]

Each entry guidance algorithm requires a flight control technique(s). The most commonly utilized and flight-proven method is bank angle modulation (BAM). Direct force control (DFC) is a new proposed technique that promises high aero maneuverability through independent modulation of angle of attack and side-slip angle. The two angles can be modulated using propulsive or non-

propulsive actuators. Although no literature exists in formulating pure DFC aerocapture guidance, hybrid bank angle and angle of attack modulated guidance has been demonstrated in Reference 4 to provide enhanced performance over standalone BAM guidance for Neptune aerocapture.

In this work, a first-of-its-kind DFC aerocapture guidance architecture is developed to assess the feasibility and robustness of Neptune aerocapture using flight-heritage blunt body aeroshells. An analytical aerodynamics model for an aeroshell derived from the Mars Science Laboratory (MSL) design is utilized in the guidance formulation. The optimal control laws for angle of attack and side-slip angle are mathematically derived from calculus of variations. Monte Carlo simulation results are presented for two distinct max L/D vehicles to assess the performance and robustness of the closed-loop DFC numerical predictor-corrector guidance. Results from a trade study between DFC and BAM guidance architectures are presented.

DIRECT FORCE CONTROL GUIDANCE

Aerodynamics Model

DFC modulates the spacecraft's angle of attack, α, and side slip angle, β, in order to orient and control the magnitude of the aerodynamic lift, L, drag, D, and side force, Q, vectors. This is in contrast to BAM where the bank angle, σ, is modulated to effectively only rotate the lift vector about the relative-velocity vector. In most bank angle aerocapture guidance studies, reaction control systems are utilized to modulate bank angle, angle of attack is trimmed at a constant value, and side slip angle is set to zero. Figure 2 provides a visualization of the flight control distinction between DFC and BAM. If horizontal, side, and vertical motion are defined by the vehicle's x, y, and z axes, then DFC provides full control authority over their respective performance as seen by the relative velocity vector components.
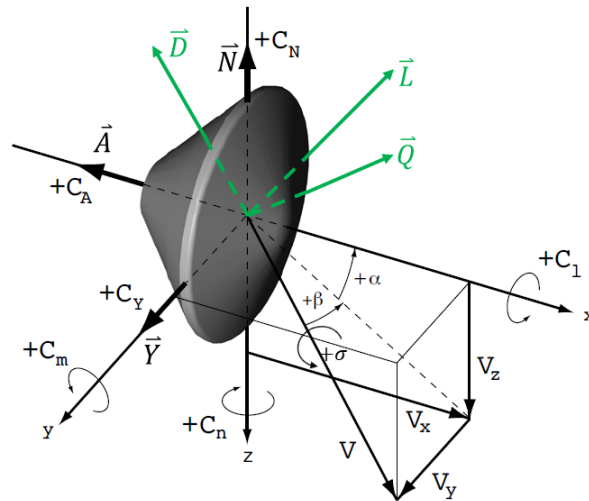

Figure 2. Visualization of aerodynamic forces generated by vehicle during aerocapture. Angle of attack, α, and side-slip angle, β, are commanded by the direct force control guidance to modulate the magnitude and direction of the wind-frame aerodynamic forces (green vectors). Bank angle modulation guidance controls the bank angle, σ, to rotate the lift vector, L, about the relative-velocity vector, V. Image adapted from Reference 8.

Figure 2 also illustrates an important distinction between body-frame, $\{\vec{A} \quad \vec{Y} \quad \vec{N}\}$, and wind-frame, $\{\vec{D} \quad \vec{Q} \quad \vec{L}\}$, aerodynamic forces. Angle of attack and side-slip angle serve as Euler rotation angles between the two frames denoted by the transformation of aerodynamic coefficients in Eq. (1). The transformation is important because the atmospheric flight equations of motion utilize wind-frame aerodynamics while the vehicle's aerodynamic model is described in the body-frame.

$$\begin{bmatrix} C_D \\ C_Q \\ C_L \end{bmatrix} = \begin{bmatrix} \cos\alpha\cos\beta & -\sin\beta & \sin\alpha\cos\beta \\ \cos\alpha\sin\beta & \cos\beta & \sin\alpha\sin\beta \\ -\sin\alpha & 0 & \cos\alpha \end{bmatrix} \begin{bmatrix} C_A \\ C_Y \\ C_N \end{bmatrix} \tag{1}$$

To obtain an analytical expression of flight-heritage blunt body aeroshell aerodynamics, the MSL aerodynamics database is utilized in this study.[9] The database provides a representation of the body-frame hypersonic aerodynamics of a 70° sphere-cone blunt body originally designed for BAM guided entry at a trim at -16° angle of attack generating an L/D of 0.24. Furthermore, the database provides capability to model the aerodynamics as functions of angle of attack and side-slip angle only, assuming insignificant influence of Mach number. Querying the database and rotating the body-frame to the wind-frame yields non-linear expressions for the aerodynamic coefficients. To achieve simplistic analytical expressions, a first-order Taylor series approximation is made about zero angle of attack and side-slip angle with the resulting L/D and side force coefficient shown by the dashed lines in Figure 3. As compared to the database, represented by solid lines, Figure 3 demonstrates that the linearization sufficiently models the vehicle L/D for a large angle of attack range and sufficiently models side force coefficient for small side-slip angles. The L/D is primarily influenced by angle of attack while the side force coefficient is primarily influenced by side-slip angle assuming small angles. These results are quite valid for application on blunt bodies as small aerodynamic angles are typically commanded. The linear aerodynamics simplifies the optimal control formulation; nevertheless, the approximation is rigorously tested against the full MSL database in the Monte Carlo simulations.
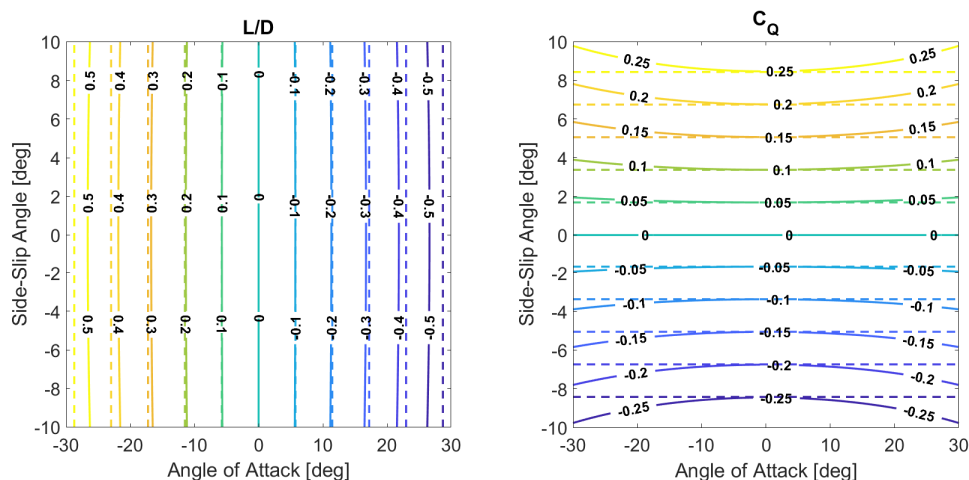
Figure 3. Comparison of vehicle L/D and side force coefficient, C_Q, vs angle of attack and side-slip angle between the linear aerodynamics model (dashed lines) and the MSL aerodynamics database (solid lines).

Guidance

The DFC guidance is formulated through the application of optimal control theory. The derivation follows a similar methodology as that presented in Reference 10 where the optimal aerocapture guidance for BAM is derived. However, the primary differences in the presented derivation are 1) the flight control method, 2) presence of side force in state dynamics, and 3) the vehicle platform.

For DFC, the guidance commands both angle of attack and side slip angle such that the two-burn scheme for periapsis raise, ΔV_1, and apoapsis correction, ΔV_2, is minimized. This cost functional, P, is derived from orbital mechanics as shown in Eq. (2) where μ is the gravitational constant of central planet, r_a is the post-aerocapture apoapsis radius, a is the post-aerocapture semi-major axis, and r_p^t and r_a^t are the targeted periapsis and apoapsis radius. The post-aerocapture apoapsis radius and semi-major axis are defined by Eq. (3) and Eq. (4) using the relative velocity magnitude, V_{exit}, position vector magnitude, r_{exit}, and flight path angle, γ_{exit}, at atmospheric exit.

$$P = |\Delta V_1| + |\Delta V_2| = \sqrt{2\mu}\left[\left|\sqrt{\frac{1}{r_a} - \frac{1}{r_a+r_p^*}} - \sqrt{\frac{1}{r_a} - \frac{1}{2a}}\right| + \left|\sqrt{\frac{1}{r_p^t} - \frac{1}{r_p^t+r_a^t}} - \sqrt{\frac{1}{r_p^*} - \frac{1}{r_a+r_p^*}}\right|\right] \quad (2)$$

$$a = \frac{\mu}{\dfrac{2\mu}{r_{exit}} - V_{exit}^2} \quad (3)$$

$$r_a = a\left[1 + \sqrt{1 - \frac{(V_{exit}r_{exit}\cos(\gamma_{exit}))^2}{\mu a}}\right] \quad (4)$$

With the utilization of a two-burn scheme, the apoapsis radius boundary condition is not explicitly enforced. However, minimization of the cost functional can be achieved by minimizing the apoapsis correction burn. This occurs when the post-aerocapture and target apoapsis radii are equal. The orbit inclination at atmospheric exit is enforced as shown in Eq. (5) where $i(\vec{x}_{exit})$ is the post-aerocapture orbital inclination computed from the state vector at atmospheric exit and i^* is the targeted inclination. The inclination is managed using separate lateral logic presented later in the paper.

$$i(\vec{x}_{exit}) - i^* = 0 \quad (5)$$

The aforementioned state vector is $\vec{x} = [r \quad \theta \quad \phi \quad V \quad \gamma \quad \psi]^T$ with components corresponding to the radial distance, r, longitude, θ, geocentric latitude, ϕ, planet-relative velocity magnitude, V, flight path angle of the planet-relative velocity vector, γ, and heading angle of the planet-relative velocity vector, ψ, respectively. The corresponding state vector dynamics governing atmospheric flight in an ellipsoid rotating planet are derived in Reference 11 and are reproduced below in Eq. (6) – Eq. (11). The application of side-slip angle introduces side force, in addition to lift, into the flight path angle and heading angle dynamics. For DFC, zero bank angle is assumed to decouple the dynamics making lift only affect flight path angle and side force only affect heading angle.

$$\dot{r} = V\sin\gamma \quad (6)$$

$$\dot{\theta} = \frac{V\cos\gamma\sin\psi}{r\cos\phi} \quad (7)$$

$$\dot{\phi} = \frac{V \cos \gamma \cos \psi}{r} \tag{8}$$

$$\dot{V} = \frac{-D(\rho, V)}{m} - g_r \sin \gamma - g_\phi \cos \gamma \cos \psi$$
$$+ \Omega^2 r \cos \phi \, (\sin \gamma \cos \phi - \cos \gamma \sin \phi \cos \psi) \tag{9}$$

$$\dot{\gamma} = \frac{1}{V} \left[\frac{L(\rho, V, \alpha)}{m} \cos \sigma + \frac{Q(\rho, V, \beta)}{m} \sin \sigma + \left(\frac{V^2}{r} - g_r \right) \cos \gamma + g_\phi \sin \gamma \cos \psi \right.$$
$$\left. + 2\Omega V \cos \phi \sin \psi + \Omega^2 r \cos \phi \, (\cos \gamma \cos \phi + \sin \gamma \cos \psi \sin \phi) \right] \tag{10}$$

$$\dot{\psi} = \frac{1}{V} \left[\frac{L(\rho, V, \alpha) \sin \sigma}{m \cos \gamma} - \frac{Q(\rho, V, \beta) \cos \sigma}{m \cos \gamma} + \frac{V^2}{r} \cos \gamma \sin \psi \tan \phi + g_\phi \frac{\sin \psi}{\cos \gamma} \right.$$
$$\left. + 2\Omega V (\tan \gamma \cos \psi \cos \phi - \sin \phi) + \frac{\Omega^2 r}{\cos \gamma} \sin \gamma \sin \phi \cos \phi \right] \tag{11}$$

Destination dependent parameters influencing the state dynamics include the planetary gravity model, modeled by g_r and g_ϕ, rotation rate, Ω, and atmosphere, modeled by ρ. Assuming the gravitational acceleration is dependent upon a radial term, g_r, latitudinal term, g_ϕ, and a gravitational potential up to the J_2 zonal term, the planetary gravity is modeled by Eq. (12) and Eq. (13) where R_e is the planet's equatorial radius. Atmospheric density, ρ, is assumed to be a function of vehicle position and is computed using the Neptune Global Reference Atmospheric Model (NeptuneGRAM).[12]

$$g_r = \frac{\mu}{r^2} \left[1 + J_2 \left(\frac{R_e}{r} \right)^2 (1.5 - 4.5 \sin^2 \phi) \right] \tag{12}$$

$$g_\phi = \frac{\mu}{r^2} \left[J_2 \left(\frac{R_e}{r} \right)^2 (3 \sin \phi \cos \phi) \right] \tag{13}$$

The aerodynamics utilized by the guidance comes from the derived blunt body linear aerodynamics model. With this approximate model and zero bank angle, angle of attack independently influences flight path angle dynamics via lift modulation as seen in Eq. (10) while side-slip angle independently influences heading angle dynamics via side force modulation as seen in Eq. (11). Because the axial coefficient, C_A, is much larger than the other two body-frame coefficients for a blunt-body and the linearization is done about zero angle of attack and side-slip angle, the coefficient of drag, C_D, and hence the drag force with this approximate model is not influenced by both angles as seen in Eq. (9). The resulting independent control authority over the state dynamics will play an important role in the optimal control formulation.

Optimal Control

To obtain the optimal control laws for angle of attack and side-slip angle, the Euler-Lagrange equations from the calculus of variations solution to the optimal control problem is utilized. The first step is the definition of the Hamiltonian, H, which for a terminal cost only problem is defined by adjoining the co-state variables, λ_r, λ_θ, λ_ϕ, λ_V, λ_γ, and λ_ψ, to the state dynamics as shown in Eq. (14).

$$H = \lambda_r \dot{r} + \lambda_\theta \dot{\theta} + \lambda_\phi \dot{\phi} + \lambda_V \dot{V} + \lambda_\gamma \dot{\gamma}(\alpha) + \lambda_\psi \dot{\psi}(\beta) \tag{14}$$

For this application, the set of admissible angles of attack and side-slip angles are explicitly constrained by a minimum and maximum value as shown by Eq. (15) and Eq. (16). Notice that the lower bounds for each angle are negative.

$$\alpha_{min} \le \alpha \le \alpha_{max}, \alpha_{min} \le 0 \tag{15}$$

$$\beta_{min} \le \beta \le \beta_{max}, \beta_{min} \le 0 \tag{16}$$

Because of the control constraints, the full Euler-Lagrange equations cannot be explicitly utilized to obtain the optimal control laws. Rather, Pontryagin's minimum principle must be applied, which indicates that the Hamiltonian must be minimized with respect to the control vector. Eq. (14) along with Eq. (10) and Eq. (11) indicate that both angle of attack and side-slip angle are *linear* with respect to the Hamiltonian. As a result, the Hamiltonian can be written in the compact form $H = H_0 + H_1\alpha + H_2\beta$ where H_1 and H_2 are two switching functions defined by Eq. (17) and Eq. (18). In these two equations, m and S_{ref} are the vehicle's mass and aerodynamic reference area, C_{L_α} is the linear coefficient of lift slope, and C_{Q_β} is the linear coefficient of side-force slope.

$$H_1 = \lambda_\gamma \left[\frac{1}{2m} \rho V S_{ref} C_{L_\alpha} \right] \tag{17}$$

$$H_2 = \lambda_\psi \left[\frac{1}{2m \cos \gamma} \rho V S_{ref} C_{Q_\beta} \right] \tag{18}$$

Applying Pontryagin's minimum principle yields a bang-bang optimal control law for angle of attack, α^*, and side slip angle, β^*, as described by Eq. (19) and Eq. (20). The cases in which either switching function equals zero for some finite time interval within the initial and final time is known as a singular arc. Using a similar proof-by-contradiction approach utilized in BAM optimal control, the singular arcs can be shown to not exist. Without loss of generality, the result below indicates that the optimal control structure for DFC aerocapture vehicles where linear aerodynamics are suitable is bang-bang and the parameter of optimization is the control switch time. Such a result is quite similar to the bang-bang optimal control structure for BAM aerocapture vehicles found in Reference 10 and thus allows for a simplistic manner of modifying existing BAM guidance algorithms to be suited for DFC application.

$$\alpha^* = \begin{cases} \alpha_{min}, & if\ H_1 > 0 \\ \alpha_{max}, & if\ H_1 < 0 \\ \in [\alpha_{min}, \alpha_{max}], & if\ H_1 \equiv 0\ in\ [t_1, t_2] \subset [t_0, t_f] \end{cases} \tag{19}$$

$$\beta^* = \begin{cases} \beta_{min}, & if\ H_2 > 0 \\ \beta_{max}, & if\ H_2 < 0 \\ \in [\beta_{min}, \beta_{max}], & if\ H_2 = 0\ in\ [t_3, t_4] \subset [t_0, t_f] \end{cases} \tag{20}$$

Numerical Predictor-Corrector

With the optimal control law structure known, the on-board trajectory optimization problem is solved utilizing a numerical predictor-corrector methodology. The existing Fully Numerical Predictor Aerocapture Guidance (FNPAG) presented in Reference 7, which is originally designed for BAM, is modified for DFC application. The algorithm consists of two phases during atmospheric

flight as illustrated by Figure 4. First, the guidance hold occurs from atmospheric entry until the sensible atmosphere is reached, which is defined by a sensed g-load greater than 0.01. Once reached, the guidance activates and Phase 1 begins. During every guidance cycle in Phase 1, the guidance determines the angle of attack switch time that minimizes the two-burn ΔV using the golden-section method while flying at maximum angle of attack. Phase 1 ends once the optimized switch time is reached. At this point, the angle of attack switches to the lower bound and Phase 2 begins. During every guidance cycle in Phase 2, the guidance determines the constant angle of attack value within the imposed bounds that minimizes the two-burn ΔV until guidance shut-off, occurring when sensed g-load is less than 0.01. This control optimization is done to mitigate trajectory dispersions caused by atmospheric density perturbations after Phase 1. After guidance shut-off, the guidance is held until atmospheric exit. In summary, the NPC predicts the trajectory by integrating the equations of motion to atmospheric exit with the univariate design parameter, either switch time or angle of attack, and corrects the design parameter by utilizing the unconstrained and parameter-bounded golden-section optimization method.
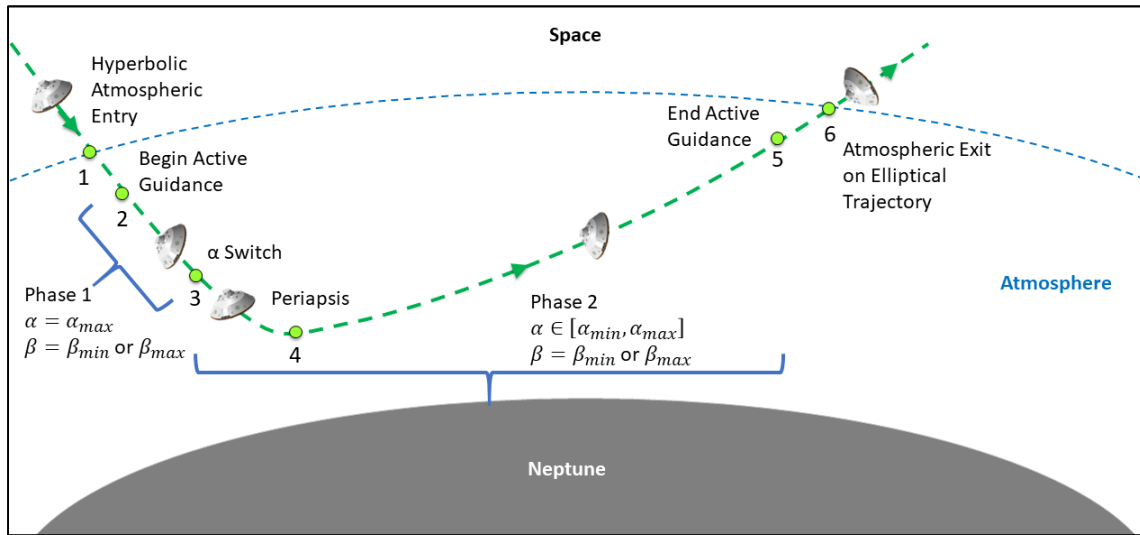
Figure 4. Two-phase direct force control Neptune aerocapture guidance.

The NPC optimization is unconstrained due to separate handling of the inclination constraint. For this separate handling, the bank angle reversal logic utilized in FNPAG is adapted to side-slip angle reversals. At guidance activation, the vehicle flies at a hold value, either maximum or minimum side-slip angle as shown in Figure 4. Using a predictive lateral logic that manages inclination error[13], side-slip angle reversals from each control bound are conducted. The number of reversals are prescribed and are utilized in the predictive logic. Although the corresponding side-slip angle switch time is not explicitly optimized, the side-slip angle lateral logic uses the fact that the derived optimal control law structure is bang-bang.

To improve the on-board atmospheric density model in the presence of dispersions, an atmospheric estimator is utilized each guidance cycle. The existing first-order fading memory filters for aerodynamic lift and drag acceleration in FNPAG are utilized to determine the corresponding density scaling factors. The estimator is extended using the same methodology to incorporate uncertainties in side force.

METHODOLOGY

Numerical Simulation

For this study, a high-fidelity three degree-of-freedom truth simulation is utilized to assess the feasibility and performance of the designed DFC guidance architecture. The Programs to Optimize Simulated Trajectories II (POST2) is employed as the trajectory propagator.[14] An oblate gravity model with harmonics up to J2 is assumed. Atmospheric interface altitude is defined at 1000 km. NeptuneGRAM is employed for the atmospheric model with dispersions. No atmospheric winds are simulated and the atmosphere is assumed to rotate with the central body. Although no active path constraints are enforced, the stagnation-point convective heat rate and integrated heat load are estimated using the Sutton-Graves relation for a reference nose radius of 1 m and Sutton-Graves coefficient of 6.79e-5 $kg^{0.5}$/m. The MSL aerodynamics model with dispersions is utilized in the propagator. The flight computer runs the guidance at 0.5 Hz. A pseudo angle of attack and side slip angle controllers are implemented limiting the rate and acceleration limits of the guidance control commands to 20 deg/s and 5 deg/s^2, respectively. The lateral logic is constrained to a maximum of three side-slip angle reversals. The vehicle inertial navigation system is assumed to have perfect state knowledge of the vehicle dynamics throughout the trajectory. This knowledge is used to estimate the current atmospheric density and update the on-board atmospheric model. For actual flight applications, the perfect knowledge assumption would be replaced by the on-board measurements from the vehicle's inertial measurement unit and flush air data sensing system. The post-aerocapture four-burn ΔV scheme associated with periapsis raise, apoapsis correction, inclination correction, and ascending node correction are computed using POST2.

Monte Carlo Setup

The Monte Carlo tests are conducted to assess the designed guidance's robustness and statistical performance to a variety of simulated dispersions, including delivery state, atmospheric density, vehicle aerodynamics, and vehicle mass.

Table 1. Monte Carlo simulated dispersions for direct force control.

Category	Variable	Nominal	±3σ or min/max	Distribution
Delivery State	Inertial entry flight path angle	-12.3° or -12.5°	From covariance	Correlated
	B-Plane angle	-176.500°	From covariance	Correlated
	Time of flight to entry interface	1.310 sec	From covariance	Correlated
	Inertial hyperbolic velocity	17.534 km/s	From covariance	Correlated
	V-infinity right ascension	-127.049°	From covariance	Correlated
	V-infinity declination	26.237°	From covariance	Correlated
Atmosphere	Random perturbation seed	1	1 to 29999	Uniform
	Fbias	0	-0.56 to 0.56	Uniform
Aerodynamics (wind-frame)	Lift coefficient	From MSL model	From MSL Uncertanty	Normal
	Drag coefficient	From MSL model	From MSL Uncertanty	Normal
	Side-force coefficient	From MSL model	From MSL Uncertanty	Normal
Mass Properties	Weight	2200 kg	From MSL Uncertanty	Normal

Table 1 lists the uncertainties and distribution types utilized in the 8001 individual Monte Carlo tests run with POST2. NeptuneGRAM is utilized to generate a uniformly distributed dispersions in atmospheric density. The full MSL model and its corresponding dispersions are simulated to rigorously test both the accuracy of the on-board linear aerodynamics model and performance of the guidance algorithm. Entry state dispersions are generated using similar correlated approach navigation performance from the previous NASA Neptune aerocapture study. In particular, the nominal inertial entry flight path angles are modified for each blunt body scenario.

NEPTUNE AEROCAPTURE

The flight-heritage blunt body vehicle analyzed in this study is analogous to MSL. However, it is assumed that the vehicle has a flight control effector, propulsive or non-propulsive, that can modulate angle of attack and side-slip angle to any corresponding angle within the imposed control limits. The limits are chosen to be within the acceptable range of accuracy for the linear aerodynamics model. Two control limit configurations for the blunt body are considered and are referred to as Scenario 1 and Scenario 2 for clarity. For Scenario 1, the angle of attack is bounded between ±20° while the side slip angle is bounded between ±5°, resulting in a maximum L/D of 0.364. For Scenario 2, the angle of attack is bounded between ±30° while side slip angle is bounded between ±5°, resulting in a maximum L/D of 0.578. The two configurations are selected to analyze the effect of increased L/D capability on aerocapture performance.

The Neptune aerocapture mission assessed is identical to the one studied in the previous NASA Neptune aerocapture study found in Reference 1. The targeted retrograde elliptical orbit, with an apoapsis of 430,000 km periapsis of 3986 km, and orbit inclination of 153.547°, is designed to enable flybys of Triton. Although not explicitly targeted, the desired longitude of ascending is 330.827°.

Corridor Definition

The traditional definition of the theoretical entry corridor used by bank angle control is constrained by a shallow and steep side. The steep side is defined as the steepest entry flight path angle which allows the vehicle to reach the target apoapsis while flying entirely full-lift vector up. The shallow side defined as the shallowest entry flight path angle which allows the vehicle to reach the target apoapsis while flying entirely full-lift vector down. Assuming angle of attack primarily controls the orientation of the lift vector for the given vehicle, full-lift vector up occurs at minimum angle and full-lift vector down occurs at maximum angle.

Using NeptuneGRAM with the nominal, minimum, and maximum atmospheric density profiles, the combined entry corridor width for Scenario 1 and Scenario 2 are determined to be 0.352° and 0.980°, respectively as shown in Table 2. Such widths are more narrow than the 1.78° bank angle width presented in Reference 4 using a 0.8 L/D slender aeroshell. The reduced L/D capabilities of the blunt bodies reduces the allowable entry corridor width.

Using the combined range, the nominal entry flight path angle is utilized as a design variable to performance-tune the nominal Monte Carlo simulations for each scenario. The resulting angles for Scenario 1 and Scenario 2 are -12.3° and -12.5°, respectively. These two values can be found in Table 1 above.

Table 2. Theoretical entry flight path angle corridor for direct force control.

| Atmosphere	Steep Side (deg)	Shallow Side (deg)	Width (deg)	Middle (deg)
Scenario 1				
Nominal	-12.771	-12.084	0.687	-12.428
Minimum	-12.896	-12.297	0.599	-12.597
Maximum	-12.649	-11.950	0.699	-12.300
Combined	-12.649	-12.297	0.352	-12.473
Scenario 2				
Nominal	-13.262	-12.085	1.177	-12.674
Minimum	-13.371	-12.185	1.186	-12.778
Maximum	-13.165	-11.809	1.356	-12.487
Combined	-13.165	-12.185	0.980	-12.675

Aerocapture Success

The feasibility of direct force control for planetary aerocapture can be assessed by the aerocapture success. For each Monte Carlo run, the resulting trajectories can be classified as either captured or uncaptured. For the former runs, further classification using an arbitrary post-aerocapture apoapsis range is typically utilized to define aerocapture success. For the latter runs, further classification can be done to distinguish hyperbolic cases and trajectories that pass below the planet radius. Although not ideal, hyperbolic cases can be corrected through propulsive burns. However, cases that pass within the planet radius cannot be corrected unless atmospheric "pop-out" burns, like those utilized in aerobraking, are integrated into the guidance logic during atmospheric flight. Since the designed guidance does not incorporate these fault protection guidance logic, aerocapture success is defined as the percentage of elliptical captured runs.

Using this criterion, the aerocapture success of Scenario1 and Scenario 2 out of 8001 Monte Carlo tests is 93.60% and 99.85%, respectively. Despite having a lower success rate, the simulation results for Scenario 1 do show promising results for DFC guidance enabling blunt-body Neptune aerocapture. Increasing success can be achieved through increasing L/D modulation capability, as shown by the results of Scenario 2. Furthermore, the results indicate that the linear aerodynamics model is both satisfactory and robust for on-board application. The aerocapture performance of the designed DFC guidance is presented in the next section.

Aerocapture Performance

The Monte Carlo orbit insertion performance of the guidance algorithm for Scenario 1 and Scenario 2 is shown in Figure 5. The guidance actively minimizes the combination of periapsis raise and apoapsis correction maneuvers, while the lateral logic minimizes the inclination error. The periapsis raise maneuver and ascending node correction are costs incurred regardless of guidance performance due to the need to raise periapsis out of the atmosphere and the precession of the ascending node due to planetary oblateness. The data suggests that increasing periapsis altitude error noticeably increases the raise maneuver ΔV while having a negative ascending node error reduces the associated correction ΔV. The lateral logic sufficiently regulates the inclination to within $\pm 0.1°$ of the targeted amount leading to a minute correction ΔV. This result demonstrates

both the validity and performance of the small side-slip angle commands utilized by the designed DFC guidance. The simulated dispersions cause a significant variation in the post-aerocapture apoapsis altitude with respect to the targeted value leading to a significant increase in the associated correction ΔV. Undershooting apoapsis significantly increases the correction ΔV cost as compared to overshooting apoapsis. Scenario 2 demonstrates smaller apoapsis altitude error on average leading to much lower correction maneuver as compared to Scenario 1. The small increase in L/D modulation capability associated with Scenario 2 contributed to significant improvement in the trajectory optimization.
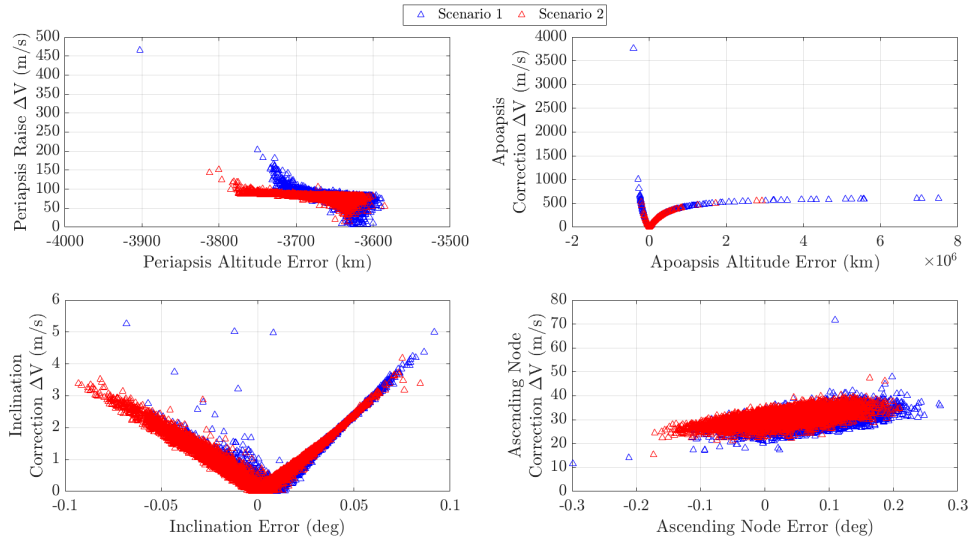
Figure 5. Monte Carlo propulsive ΔV magnitude vs insertion error for periapsis altitude, apoapsis altitude, inclination, and longitude of ascending node corrections.

A histogram of the periapsis plus apoapsis and total ΔV cost for each vehicle is shown in Figure 6. The former cost is representative of the DFC guidance trajectory optimization performance while the latter cost is representative of the additional ΔV required after aerocapture for full orbit insertion. Due a significantly lower apoapsis error, the majority of Scenario 2 simulation cases outperform Scenario 1 in terms of each ΔV cost. Furthermore, the increase in L/D capability with Scenario 2 significantly reduces the statistical spread of the ΔV costs by more than an order of magnitude.
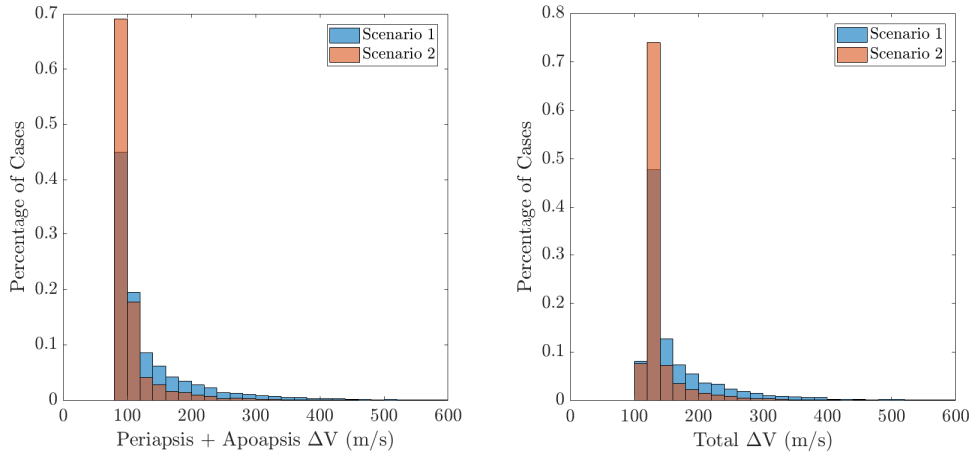
Figure 6. Monte Carlo histograms for periapsis raise + apoapsis correction ΔV and total correction ΔV cost.

COMPARISON TO BANK ANGLE MODULATION

The previous section of this paper demonstrated the viability and robustness of Neptune aerocapture using a flight-heritage blunt body employing DFC. The existing NASA Neptune aerocapture study demonstrated similar viability and robustness of Neptune aerocapture using slender bodies employing BAM. Consequently, two distinct vehicle architectures for Neptune aerocapture are present: 1) blunt-body DFC and 2) slender-body BAM. Architecture 1 requires significant technology maturation in flight control surfaces for modulating angle of attack and side-slip angle while Architecture 2 requires technology maturation in slender aeroshells. Given these technological requirements, the natural questions arises of what is the technology benefit of one architecture over the other. This question can be addressed through trade studies on the potential flight control techniques and aeroshell configuration options. Consequently, the results presented in this section provide a first-cut assessment of the aerocapture technology trade space.

A means to facilitate the trade study is the aerocapture guidance architecture. Although the guidance may employ different control methods, the core algorithms are generally the same. For the same optimization problem setup, the derived optimal control structure for DFC is identical to that derived for BAM. The same closed-loop numerical predictor-corrector algorithm is utilized for the on-board guidance. Because of these similarities, the same Neptune aerocapture mission is analyzed for a BAM guidance. Using Reference 15, a slender ellipsled aeroshell trimmed at 40° angle of attack, corresponding to L/D of 0.8, is analyzed. This vehicle configuration, adapted from the NASA Neptune aerocapture systems study, is referred to as Scenario 3 for clarity. The numerical simulation setup is nearly identical to that utilized by DFC simulations. Control specific modifications include a maximum of three bank angle reversals for the lateral logic, pseudo controller limiting the bank angle rate and acceleration limits to 20 deg/s and 5 deg/s^2, and bank angle control limits of ±165°. The prescribed Monte Carlo dispersions are identical except for the aerodynamics and mass, which are modified to be representative of the analyzed ellipsled, as well as entry flight path angle, which come from the study. A summary of these modifications are shown in Table 3.

Table 3. Modified Monte Carlo simulated dispersions for bank angle modulation.

Category	Variable	Nominal	±3σ or min/max	Distribution
Delivery State	Inertial entry flight path angle	-12.818°	From covariance	Correlated
Aerodynamics (wind-frame)	Lift coefficient	1.124	±0.1707	Normal
	Drag coefficient	1.405	±0.1193	Normal
Mass Properties	Weight	2200 kg	±10%	Normal

Table 4. Monte Carlo statistics for direct force control and bank angle modulated aerocapture at Neptune.

Parameter	Mean	3σ	1st percentile	50th percentile	99th percentile
Direct Force Control - Scenario 1					
Apoapsis Error, x10^3 km	58.035	821.524	-100.155	5.255	693.970
Inclination Error, deg	0.016	0.064	-0.035	0.017	0.063
Periapsis + Apoapsis ΔV, m/s	136.606	275.384	83.425	102.451	468.261
Inclination + Node ΔV, m/s	31.494	9.381	23.827	31.521	38.968
Total ΔV, m/s	168.100	274.261	113.602	135.332	497.741
Peak deceleration, g	7.028	3.213	4.753	6.966	9.822
Peak conv. heat rate, W/cm^2	3426.217	927.093	2869.254	3397.081	4239.684
Integrated heat load, kJ/cm^2	502.162	75.645	459.495	498.014	591.757
Direct Force Control - Scenario 2					
Apoapsis Error, x10^3 km	18.058	223.131	-24.715	1.096	255.826
Inclination Error, deg	-0.004	0.079	-0.068	-0.003	0.052
Periapsis + Apoapsis ΔV, m/s	107.927	112.660	84.015	97.583	280.296
Inclination + Node ΔV, m/s	31.947	8.146	25.415	31.962	38.170
Total ΔV, m/s	139.874	111.131	114.173	130.160	308.183
Peak deceleration, g	7.028	3.213	4.753	6.966	9.822
Peak conv. heat rate, W/cm^2	3856.788	1192.177	3040.000	3832.026	4881.821
Integrated heat load, kJ/cm^2	486.859	52.924	451.382	486.440	538.290
Bank Angle Modulation – Scenario 3					
Apoapsis Error, x10^3 km	10.084	116.877	-73.468	4.700	124.979
Inclination Error, deg	0.045	0.486	-0.573	0.029	0.403
Periapsis + Apoapsis ΔV, m/s	121.908	102.165	83.595	112.688	242.671
Inclination + Node ΔV, m/s	67.795	38.158	38.747	65.908	101.994
Total ΔV, m/s	189.703	102.067	141.714	182.189	308.046
Peak deceleration, g	12.643	5.201	9.102	12.524	17.260
Peak conv. heat rate, W/cm^2	4316.322	892.906	3676.385	4307.250	5053.537
Integrated heat load, kJ/cm^2	465.786	75.793	412.117	464.917	530.161

The Monte Carlo simulation statistics for the DFC datasets, Scenario 1 and 2, and the BAM dataset, Scenario 3, are summarized in Table 4. Statistics include orbit insertion performance in terms of apoapsis altitude and inclination error, correction ΔV burns, peak deceleration, peak convective heating, and integrated heat load. The simulation statistics demonstrate that the designed DFC guidance applied to both blunt-body vehicles is sufficiently robust to overcome uncertainties in delivery state, vehicle aerodynamics, and atmospheric density. To achieve full orbit insertion for the analyzed Neptune mission using Scenario 1 or Scenario 2, the 99th percentile total ΔV required is 498 m/s and 308 m/s, respectively. The DFC vehicles exhibit significantly better lateral logic in terms of a lower inclination error and corresponding out-of-plane ΔV cost. The importance of this latter burn to the total ΔV cost is also exhibited in the statistics. The corresponding burn for the DFC vehicles accounts for less than 15% of the total cost as compared to the 33% demonstrated by the BAM slender vehicle. Despite having a lower L/D modulation capability, Scenario 2 apoapsis error and corresponding ΔV is on par with the performance of Scenario 3. This result demonstrates that DFC can enable Neptune aerocapture with flight-heritage blunt bodies without significantly compromising performance as compared to BAM slender bodies. Although no active path constraints are enforced in the simulations, the peak deceleration, peak convective heat rate, and integrated heat load values are significant. The aero heating parameters are similar between the DFC and BAM vehicles; yet, the peak deceleration is 50% lower for DFC. This finding indicates that DFC can be enable a significant reduction in vehicle structural requirements.

CONCLUSIONS

The application of a direct force control guidance for planetary aerocapture at Neptune is investigated in this work. The investigation included the formulation of an analytical aerodynamics model for a flight-heritage blunt body aeroshell as well as the derivation of optimal control laws associated with angle of attack and side-slip angle modulation. The closed-loop guidance is formulated using a numerical predictor-corrector algorithm. Blunt-body aerocapture employing direct force control with two different L/D modulation capabilities are investigated. The theoretical entry corridor as well as the algorithm performance under perturbations in aerodynamics, atmospheric density, and entry state for each scenario is presented. The Monte Carlo simulation results demonstrate the viability and robustness of direct force control blunt-body aerocapture, enabling 99.85% successful science orbit insertion within a 310 m/s total ΔV budget for periapsis raise, apoapsis, inclination and ascending node adjustments. Comparisons to slender body bank angle modulated guidance indicate that direct force control employed on blunt bodies can both enable similar aerocapture performance with lower L/D modulation capability and can substantially reduce vehicle g-loading.

The first-of-its-kind results presented for direct force control demonstrates the relevance of the flight control technique as an enabling and enhancing aerocapture technology. Conducting further trade studies on the different flight controls, including drag modulation, flight effectors, including non-propulsive ones, and aeroshell configuration options, including deployable decelerators, at other planetary destinations is warranted. As demonstrated in this paper, the modular guidance architecture can be utilized as the catalyst in performing such further studies.

ACKNOWLEDGMENTS

REFERENCES

[1] M. K. Lockwood et al., "Aerocapture Systems Analysis for a Neptune Mission," NASA/TM-2006-214300, 2006.

[2] Lockwood, M. K., "Neptune Aerocapture Systems Analysis." AIAA 2004-4951, AIAA Atmospheric Flight Mechanics Conference and Exhibit, Providence, RI, 2004.

[3] Hill, O., "An adaptive guidance logic for an aeroasisted orbital transfer vehicle." AAS 83-357.

[4] Masciarelli, J. P., Westhelle, C. H., and Graves, C. A., "Aerocapture Guidance Performance for the Neptune Orbiter." AIAA 2004-4954, AIAA Atmospheric Flight Mechanics Conference and Exhibit, Providence, RI, 2004.

[5] Masciarelli, J.; "Aerocapture Guidance Algorithm Development and Testing." 2007 NASA Science Technology Conference, College Park, MD, 2007.

[6] Powell, R. W., "Numerical Roll Reversal Aerocapture and Precision Landing Guidance Algorithms for the Mars Surveyor Program 2001 Missions." AIAA 98-4574, AIAA Atmospheric Flight Mechanics Conference, Boston, MA, 1998.

[7] Webb, K. D., Lu, P., and Dwyer Cianciolo, A. M., "Aerocapture Guidance for a Human Mars Mission." AIAA 2017-1900, AIAA Guidance, Navigation, and Control Conference, Grapevine, TX, 2017.

[8] Schoenenberger, M., Cheatwood, F. M., and Desai, P., "Static Aerodynamics of the Mars Exploration Rover Entry Capsule." AIAA 2005-56, 43rd AIAA Aerospace Sciences Meeting and Exhibit, Reno, NV, 2005.

[9] Dyakonov, A., Schoenenberger, M., and Van Norman, J., "Hypersonic and Supersonic Static Aerodynamics of Mars Science Laboratory Entry Vehicle." AIAA 2012-2999, 43rd AIAA Thermophysics Conference, New Orleans, LA, 2012.

[10] Lu, P., Cerimele, C. J., Tigges, M. A., and Matz, D. A., "Optimal Aerocapture Guidance." Journal of Guidance, Control, and Dynamics, Vol. 38, No. 4, April 2015, pp. 553–565.

[11] Miele, A., Zhao, Z. G., and Lee, W. Y., "Optimal trajectories for the Aeroassisted Flight Experiment. Part 1: Equations of motion in an Earth-fixed system." NASA-CR-186134, 1989.

[12] Justus, C. G., Duval, A., and Keller, V. W., "Atmospheric Models for Aerocapture Systems Studies." AIAA 2004-4952, AIAA Atmospheric Flight Mechanics Conference and Exhibit, Providence, RI, 2004.

[13] Smith, K. M., "Predictive lateral logic for numerical entry guidance algorithms." AAS 16-216, 26th AAS/AIAA Space Flight Mechanics Meeting, Napa, CA, 2016.

[14] S.A. Striepe et al., "Program To Optimize Simulated Trajectories (POST II): Volume 2, Utilization Manual." Martin Marietta Corporation, 2004.

[15] Edquist, K., Prabhu, R., Hoffman, D., and Rea, J., "Configuration, Aerodynamics, and Stability Analysis for a Neptune Aerocapture Orbiter." AIAA 2004-4953, AIAA Atmospheric Flight Mechanics Conference and Exhibit, Providence, RI, 2004.